npj | clean water

Article

Published in partnership with King Fahd University of Petroleum & Minerals

https://doi.org/10.1038/s41545-025-00496-w

Nanoparticle-encapsulated organo-magnetogels: crosslinked network for broad-spectrum pollutant removal

Sanjeevi Prasath Sridhar[1], Sudha Uthaman[1], Logesh Kumar Pandurangan[1], Armin Kriele[2], Debasish Saha[3], Baohu Wu[3], Velraj Parthiban[1], Janaki Vembu Murugesan[1], Balachandar Vijayakumar[1], Stephan Förster[4,5], Aurel Radulescu[3] & Brijitta Joseph[1,3] ✉

In this contribution, we report the synthesis of a poly(4-vinylpyridine)-reduced graphene oxide-magnetite (P4VP-rGO-Fe_3O_4) organo-magnetogel (OMG), designed for high-performance pollutant adsorption. In the OMG, rGO and Fe_3O_4 nanoparticles are in situ encapsulated during the chemical cross-linking of the 4-vinylpyridine polymer. The adsorption performance of OMG was evaluated using three model water pollutants, viz., organic dyes, heavy metal ions, and waterborne pathogens. The equilibrium adsorption capacity exceeded 400 mg/g for the organic dyes. Beyond dye removal, the OMG also adsorbed heavy metal ions, such as AsO_2^-, Pb^{2+}, $Cr_2O_7^{2-}$, and Cd^{2+} ions, with removal efficiencies exceeding 60% and adsorption capacities exceeding 200 mg/g. The OMG also exhibited remarkable antibacterial activity against *E. coli* and *S. Typhi*, with almost zero viability for *S. Typhi*. The OMG promises a broad-spectrum applicability in wastewater treatment, offering a sustainable and efficient solution for water decontamination.

Industrial effluents, agricultural runoffs, and untreated domestic wastewater contaminate the water bodies, degrade water quality, and pose significant health risks and aquatic damage. In developing countries, this issue is further aggravated due to the lack of stringent regulations to control the discharge of contaminants into water bodies. According to the UN-Water, the inter-agency of the UN responsible for work on water and sanitation, ~3.5 million people die each year due to inadequate water supply, sanitation, and hygiene. One major contributor to water contamination is the textile industry, which discharges organic pollutants such as azo, reactive, and disperse dyes[1–5]. Industrial discharges and mining releases heavy metals[6–9] such as lead (Pb), cadmium (Cd), chromium (Cr), mercury (Hg), and arsenic (As) into water bodies. Pollutants often detected in water bodies, such as microplastics[10,11], pharmaceuticals[12,13], pesticides[14], and endocrine-disrupting compounds[15], have already left their footprints in the food chain and human bodies[16,17]. Waterborne pathogenic bacteria are also a cause for critical concern. For example, pathogens such as *Salmonella enterica* serovar Typhi (*S. Typhi*)[18] and *Escherichia coli (E. coli)*[19] can cause typhoid fever and gastrointestinal illnesses. Therefore, addressing the water contaminants has received significant attention, driving the development of improved water treatment technologies such as adsorption, advanced oxidation processes, membrane filtration, photodegradation, etc[20–34]. To this end, various adsorbents, such as advanced porous materials like mesoporous silica[35,36] with exceptionally high surface areas, metal-organic frameworks[37–41], covalent organic frameworks[38,42–46], biochar[47,48], and polymers[11,49–52], have been employed to remove a wide range of pollutants.

Adsorption of contaminants onto gel adsorbents is an effective technique for treating contaminated wastewater[24,53–62]. Polymer-based organogels[20,21,23] are solid or semi-solid materials formed by cross-linking polymer chains in organic solvents. This results in a 3-D gel network with high mechanical strength and tunable properties. In a previous study, we reported the synthesis of organogels derived from poly(styrene-*block*-4-vinylpyridine)[21] and poly(N-isopropylacrylamide-*block*-4-vinylpyridine)[20]. These organogels demonstrated notable capabilities, including adsorption specificity towards anionic dyes, heavy metal anions, and antibacterial activity. Building on these findings, this study presents the development of a chemically cross-linked poly(4-vinylpyridine)-reduced graphene oxide-magnetite (P4VP-rGO-Fe_3O_4) OMG that encapsulates magnetite (Fe_3O_4) nanoparticles and reduced graphene oxide (rGO) as functional components. While P4VP-based materials such as block copolymers and hydrogels loaded with nanoparticles have been explored, the current study introduces

[1]Centre for Nanoscience and Nanotechnology, Sathyabama Institute of Science and Technology, Chennai, India. [2]German Engineering Materials Science Centre (GEMS) at Heinz Maier-Leibnitz Zentrum (MLZ), Helmholtz-Zentrum Hereon GmbH, Garching, Germany. [3]Jülich Centre for Neutron Science (JCNS-4), Heinz Maier-Leibnitz Zentrum (MLZ), Forschungszentrum Jülich GmbH, Garching, Germany. [4]Jülich Centre for Neutron Science (JCNS-1/IBI-8), Forschungszentrum Jülich, Jülich, Germany. [5]Institute of Physical Chemistry, RWTH Aachen University, Aachen, Germany. ✉e-mail: b.joseph.boniface@fz-juelich.de; brijitta@live.com

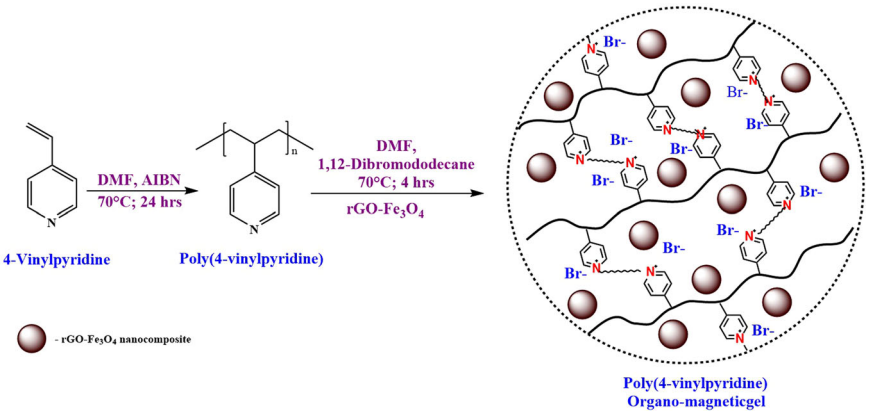

Fig. 1 | Chemical crosslinking of the P4VP homopolymer and encapsulation of rGO-Fe_3O_4 composite. Scheme for synthesizing P4VP-rGO-Fe3O4 organo-magnetogel.

an OMG composed of homopolymeric P4VP gel network, encapsulated with rGO and Fe_3O_4 nanoparticles. This formulation results in a soft yet porous OMG, with a surface area of ~189.561 m^2/g. The P4VP-rGO-Fe_3O_4 OMG combines the unique properties of both organogels and magnetogels, offering distinct advantages over the individual systems. In contrast to magnetogels, which often lack sufficient functional groups for specific adsorption, the P4VP-rGO-Fe_3O_4 OMG benefits from the tunable chemistry of the gel network, allowing the incorporation of functional groups for tailored applications.

Results and discussion

Synthesis and characterization of the OMG

The first step in preparing the P4VP-rGO-Fe_3O_4 OMG is the ball-milling of a 3:1 ratio mixture of rGO and Fe_3O_4 for 6 h to obtain a composite of rGO-Fe_3O_4. Next, 10 wt% 4-vinylpyridine, 2 wt% of rGO-Fe_3O_4 composite, and 200 mg of 1,12-dibromododecane (DBD) were dissolved in dimethylformamide (DMF). After thorough mixing by sonication, the solution was degassed through three freeze-pump-thaw cycles. Chemical crosslinking was achieved by heating the polymer solution at 70 °C for 4 h under an inert atmosphere, forming the P4VP-rGO-Fe_3O_4 gel network. The synthesis scheme for the P4VP-rGO-Fe_3O_4 OMG is illustrated in Fig. 1. Gelation was not observed at lower concentrations of 4-vinylpyridine. Details of the preliminary gelation studies are provided in the supplementary information and the Fig. S1. The same methodology was used for preparing P4VP organogel, P4VP-rGO organogel, and P4VP-Fe_3O_4 magnetogel. The gel encapsulated with Fe_3O_4 is termed magnetogel.

Figure S2 shows the ^{1}H NMR spectra of the P4VP polymer and the crosslinked P4VP organogel, recorded under identical instrumental conditions. In the P4VP organogel, the chemical shifts (δ) for the pyridine ring protons were observed at δ = 7.7–8.5 ppm, and the δ for the aliphatic -CH_2 groups occur at 1.1–2.8 ppm. For the P4VP organogel, additional chemical shifts at δ = 4.5–5.07 ppm (-$(CH_2)_n$-N) confirm the bridging between the pyridine group of the vinylpyridine and DBD. We performed scanning electron microscopy (SEM) imaging in the environmental SEM (ESEM) mode to observe the gel morphology and the distribution of the rGO, Fe_3O_4, and their nanocomposites within the P4VP network. The ESEM images of the P4VP organogel, P4VP-rGO organogels, P4VP-Fe_3O_4 magnetogel, and P4VP-rGO-Fe_3O_4 OMG are shown in Fig. 2a–d, respectively. The P4VP organogel shows a homogeneous surface (Fig. 2a); adding rGO and Fe_3O_4 resulted in their homogeneous distribution within the gel matrix, indicating the successful encapsulation of rGO and Fe_3O_4 into the gel network. Figure 2e shows the area chosen for EDX imaging and the respective colour-coded elemental mapping; the colours blue, green, and brown represent elements carbon, oxygen, and iron, respectively. The elemental mapping confirms the uniform distribution of the constitutional elements, corroborating the homogeneous encapsulation of rGO-Fe_3O_4 composites within the OMG. Figure 2f shows photographs of knife-cut pellets of the gels.

The magnetic properties of the Fe_3O_4 and the P4VP-rGO-Fe_3O_4 OMG were evaluated using vibrating sample magnetometry (VSM) (Figure S3); both the samples exhibited superparamagnetic behaviour. For Fe_3O_4, the coercivity (Hc) at B = 0 was 0 Oe, and the intrinsic coercivity (Hci) at m = 0 was 11.79 Oe, indicating negligible resistance to demagnetization typical of superparamagnetic nanoparticles. The saturation magnetization (Ms) was 1.09 emu for a 20 mg sample, corresponding to a specific magnetization of 54.72 emu/g, which is lower than ~92 emu/g for bulk magnetite[63,64] due to nanoscale size effects, surface spin disorder, or due to nonmagnetic components. The retentivity (Mr) was 0.017 emu, reflecting minimal residual magnetization. Similarly, the P4VP-rGO-Fe_3O_4 OMG exhibited very soft magnetic behavior with Hc = 0 Oe, intrinsic coercivity Hci = 6.54 Oe, and a much lower Ms of 0.16 emu for 16 mg (9.69 emu/g) because of dilution by the nonmagnetic P4VP gel matrix and rGO. The OMG retentivity was low at 0.001 emu. The combination of low coercivity, low remanence, and moderate Ms in both Fe_3O_4 and the P4VP-rGO-Fe_3O_4 OMG confirms the superparamagnetic nature of the Fe_3O_4 nanoparticles.

Small-angle X-ray scattering (SAXS) studies

Results obtained from small-angle X-ray scattering (SAXS) measurements for the pure components of rGO, Fe_3O_4, P4VP organogel, and the ternary OMG are shown in Fig. 3a. The scattering data of the binary systems, P4VP-rGO, P4VP-Fe_3O_4, and rGO-Fe_3O_4 composite, are shown in Fig. 3b. Details of the data fitting models are provided in the supplementary information. In Fig. 3a, the scattering profile of P4VP organogel shows two length scales, with a change in the slope at q~0.013 $Å^{-1}$. The model fitting using Fisher–Burford (FB) yields an R_g of 20.3 Å for each subunit of the gel and a fractal dimension, D_f of 2.7, suggesting a mass-fractal-like structure. However, the obtained D_f is much higher than the typical diffusion-limited cluster aggregation (DLCA) and reaction-limited cluster aggregation (RLCA) but is closer to the ballistic-particle cluster aggregation (BPCA). Simulations show that in BPCA, particles/clusters are spread out in space. Collisions occur when particles move together as a cluster, causing them to coalesce and form a dense cluster[65]. The number of nearest neighbors in BPCA is much higher than the DLCA, reaching a fully coalesced state much faster[66]. In the P4VP-rGO-Fe_3O_4 OMG, the Porod exponent obtained in the low-q regime is higher than 3, suggesting the presence of larger inhomogeneities with fractal morphologies. These large inhomogeneities represent highly compact and densely cross-linked regions within the gel network[67].

For rGO, unlike the structure reported in the literature, a clear mid-q cut-off is observed at q~0.07 $Å^{-1}$ with an equivalent R_g of ~52 Å. A q^{-4} dependence for rGO is obtained, which implies high surface roughness, compactness, and crumpled morphology[68]. For Fe_3O_4 nanoparticles using the spherical form factor combined with a fractal model, a mean radius of 52.1 Å particles with a broad size distribution is obtained. The linearity observed in the low-q region is fitted with a slope of 3.06, suggesting a compact surface fractal-like morphology. The scattering obtained for P4VP-rGO-Fe_3O_4 OMG is similar to the P4VP-organogel but very different from

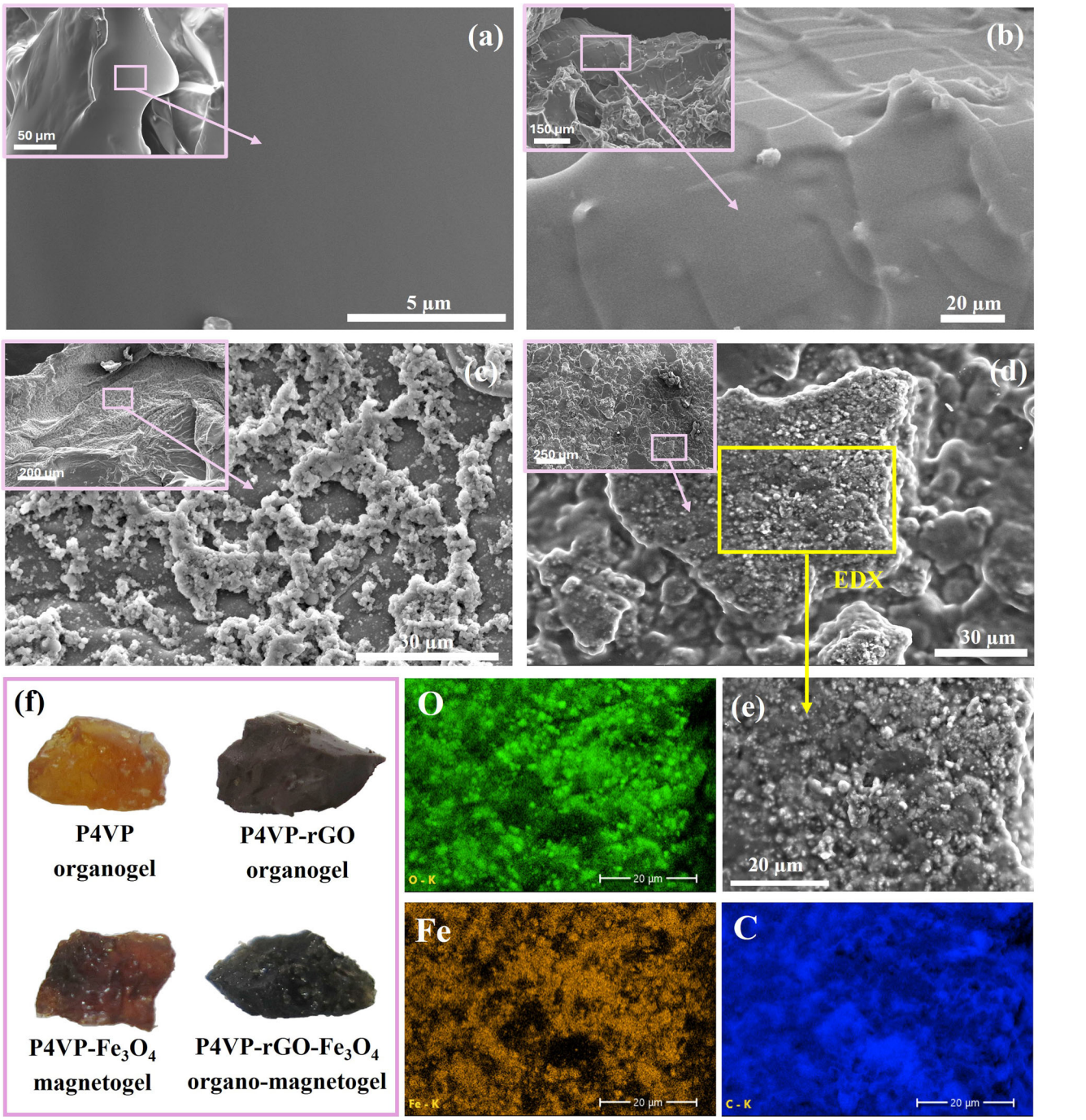

Fig. 2 | Morphology, elemental mapping and photographs of the gels. ESEM images (**a**) P4V(P organogel, **b** P4VP-rGO organogels, **c** P4VP-Fe_3O_4 magnetogel, and (**d**) P4VP-rGO-Fe_3O_4 OMG, **e** enlarged area of **d** chosen for EDX and the respective elemental mapping, and **f** photographs of all the gels.

the individual components of rGO and Fe_3O_4 nanoparticles. The R_g of the subunit of OMG increased from 21.3 Å to 51.5 Å plausibly to accommodate more rGO and Fe_3O_4 nanoparticles inside the gel network. The D_f obtained from the FB fitting is marginally lower compared to the typical dimension of a BPCA cluster, but much higher than that of the fractal dimension of a DLCA cluster. This suggests that the gel network slightly expands to accommodate rGO and Fe_3O_4 nanoparticles within the OMG network than the pristine P4VP organogel network.

We analyzed the binary gel systems to understand the role of individual components in Fig. 3b. The scattering intensity of each binary system is completely different from the scattering of the individual components, and the linear superposition of scattering data from each component cannot be considered. This implies strong interactions between the components, and suitable models must be used for the data fitting. The binary mixture of Fe_3O_4 nanoparticles encapsulated within the P4VP organogel shows an explicit mid-q cutoff with a linear build-up in the scattering intensity in the low-q regime. The scattering data fitted with the spherical form factor with a broad size distribution gives a mean radius of 51.9 Å, which is very close to the mean radius of pure Fe_3O_4 nanoparticles. Since there is no clear cutoff in the higher-q regime, which is related to each subunit of the gel network, it might be stated that the subunit of the gel network has been expanded to accommodate more Fe_3O_4 nanoparticles inside the network. The D_f of these binary components is observed to be 2.75, which is very close to the dimensionality of the P4VP organogel network but smaller than the surface

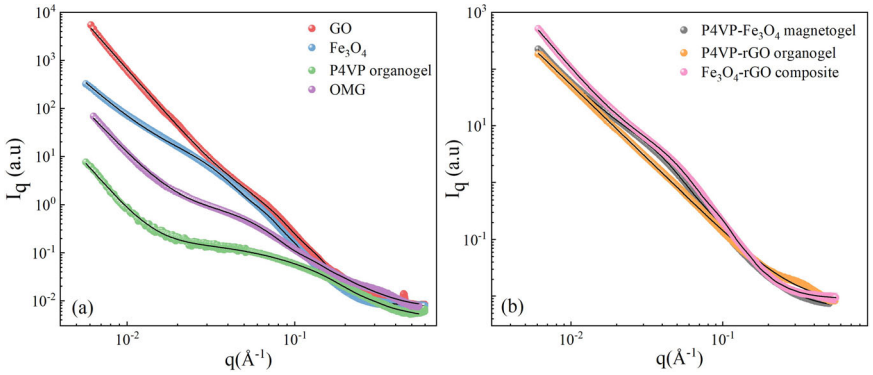

Fig. 3 | SAXS curves of the gels and their respective constituents. SAXS data of (**a**) P4VP organogel, rGO, Fe_3O_4 nanoparticles, and the ternary OMG, **b** binary system of P4VP-Fe_3O_4 magnetogel, P4VP-rGO organogel, and rGO-Fe_3O_4 composite. The solid black lines represent the model fitting of scattering data.

fractal structure of pure Fe_3O_4 nanoparticles. Thus, the result suggests that in the presence of Fe_3O_4 nanoparticles, P4VP gels maintain their gel network structure, only exhibiting subunit expansion to accommodate more nanoparticles in the network.

In the case of P4VP-rGO organogel, the scattering contribution from the subunit of the P4VP organogel and from the individual rGO building block completely disappeared in the SAXS data of their binary mixture. However, the linearity in the low-q is 2.59, which is similar to the D_f of the P4VP organogel network. This implies that the P4VP-rGO organogel maintains the branching of its gel network in larger dimensions, even in the presence of rGO. It might be possible that while interacting with rGO, which also possesses a large layer structure, the phase boundary between these two components was lost entirely, leading to the disappearance of the scattering cutoff in the mid-q from the individual subunits. On the other hand, the scattering from the rGO-Fe_3O_4 nanoparticles system is dominated by the scattering features of Fe_3O_4 nanoparticles. The ball milling of rGO and Fe_3O_4 nanoparticles reduces their size while maintaining the surface fractal-like morphology similar to that of the Fe_3O_4 nanoparticles. Different parameters obtained from the fittings are listed in Table S1.

Dye adsorption Studies

The dye adsorption properties of the gels were studied using a 2 wt% gel pellet and aqueous solutions containing 0.1 g/L dye. UV-vis spectra were recorded for all the gels after the dye solution was kept in contact with the gels for 60 min. The chemical structure of the model dye pollutants is provided in Fig. S4, and the details of the UV-vis peak maxima for all the dyes are provided in the supplementary information. The UV-vis spectra of the dye solutions after 60 min of contact with the gels are presented in Fig. 4a–h. P4VP organogel is a cationic gel; thus, its adsorption is highly selective towards anionic dye molecules. This selectivity is evident in Fig. 4f, g, where the adsorption of cationic dyes such as malachite green (MG), neutral red (NR), and alcian blue (AB) by the P4VP organogel is almost nil. In contrast, anionic dyes like methyl orange (MO), methyl red (MR), bromocresol green (BG), and eosin blue (EB) exhibit significantly higher adsorption, suggesting a much higher affinity between the protonated pyridine groups of P4VP and negatively charged dye molecules. Among the P4VP-rGO and P4VP-Fe_3O_4 gels, the P4VP-rGO organogel demonstrates better adsorption. This enhanced adsorption in P4VP-rGO arises from electrostatic attraction, hydrogen bonding, and the π–π interactions[69–71]. In the case of P4VP-Fe_3O_4 magnetogel, the dye removal occurs via surface charge interactions and complexation.

Compared to all other gels, the P4VP-rGO-Fe_3O_4 gel exhibited superior adsorption capability for both anionic and cationic dyes. The dye solutions kept in OMG appeared almost water-like within 60 min of contact with the gel (Fig. 4a–g). The exceptional dye adsorption performance of OMG can be attributed to the electrostatic interaction between the dye molecules and OMG; the large surface areas of rGO and Fe_3O_4, along with their intrinsic contribution, further enhance the dye uptake. The supplementary video S. Video 1 shows the action of the P4VP-rGO-Fe_3O_4 OMG towards the adsorption of the MG dye. Note that no separate magnetic pellets were added to the dye solution. Instead, the magnetite encapsulated within the gel allows it to respond to the magnetic field generated by a standard laboratory magnetic stirrer. Under the influence of this field, the gel pellets exhibit rotational motion, facilitating enhanced interaction with the dye solution without the need for additional magnetic components. Remarkably, the gel demonstrated excellent structural integrity, withstanding continuous stirring at 1000 rpm for several hours without any signs of degradation or fragmentation. This robust performance highlights the P4VP-rGO-Fe_3O_4 OMG's mechanical stability and suitability for repeated adsorption-desorption cycles under dynamic conditions. The presence of magnetite in the gel simplifies the recovery of the gel pellets from the desorbed solution (S. Video 2), thereby enabling easy recovery of the adsorbent using an external magnetic field. The photograph of the dye solutions before and after adsorption by the P4VP-rGO-Fe_3O_4 OMG is shown in Fig. 4i. Notably, the adsorption studies utilized only a minimal amount of the gel (2 wt%), highlighting the OMG's efficiency. Increasing the OMG quantity could further reduce the required adsorption time, as evidenced in the supplementary video S. Video 1, where the dye adsorption of MO was drastically reduced to ~30 min for a 3 wt% pellet of OMG. Adsorption studies were also performed using mixtures of anionic and cationic dyes Fig. 4h. Unlike the P4VP gel, which is selective for anionic dyes, the OMG can adsorb both cationic and anionic dyes at the same rate, similar to the adsorption in individual anionic and cationic dye solutions.

Adsorption capacity

The equilibrium adsorption capacity of the P4VP, P4VP-Fe_3O_4, P4VP-rGO, and P4VP-rGO-Fe_3O_4 gels was calculated using Eq. 1. Figure 5a shows the equilibrium dye adsorption capacities ($Q_{e(MO\ dye)}$) of the gels (a) P4VP, (b) P4VP-Fe_3O_4, (c) P4VP-rGO, and (d) P4VP-rGO-Fe_3O_4 for the anionic MO dye after 24 h of contact with the gels. The MO adsorption, the equilibrium adsorption capacity $Q_{e(MO\ dye)}$ was found to be 196, 222, 303, and 444 mg/g, respectively, for the P4VP, P4VP-Fe_3O_4, P4VP-rGO, and P4VP-rGO-Fe_3O_4 gels. A similar trend is noted for all the other dyes investigated in this study. Figure 5b shows that the adsorption capacity of P4VP organogel is ~195 mg/g for all the anionic dyes. Note that we have not provided the equilibrium adsorption capacity for MG, NR, and AB for P4VP, as P4VP is selective towards anionic dyes only. The P4VP-rGO organogel followed MO > MR > EB > MG > BG > NR > AB, highlighting the enhanced interactions introduced by the rGO sheets. The P4VP-Fe_3O_4 magnetogel showed adsorption capacities for EB > MO > MR > BG > MG > NR > AB. Finally, the P4VP-rGO-Fe_3O_4 OMG showed a preferential sequence of MO = MG > EB > NR > BG > MR > AB, reflecting the combined action of rGO and Fe_3O_4 in enhancing the adsorption capacity. Figure 5c shows the dye removal efficiency (%) of the P4VP-rGO-Fe_3O_4 OMG for all the dyes investigated in the study. The removal efficiencies are calculated based on Eq. 2. Even after 10 cycles, MO achieves over 95% dye removal, while EB, BG, MR, MG, NR, and AB exceed 92%, 91%, 89%, 88%, 93%, and 86%, removal efficiencies respectively.

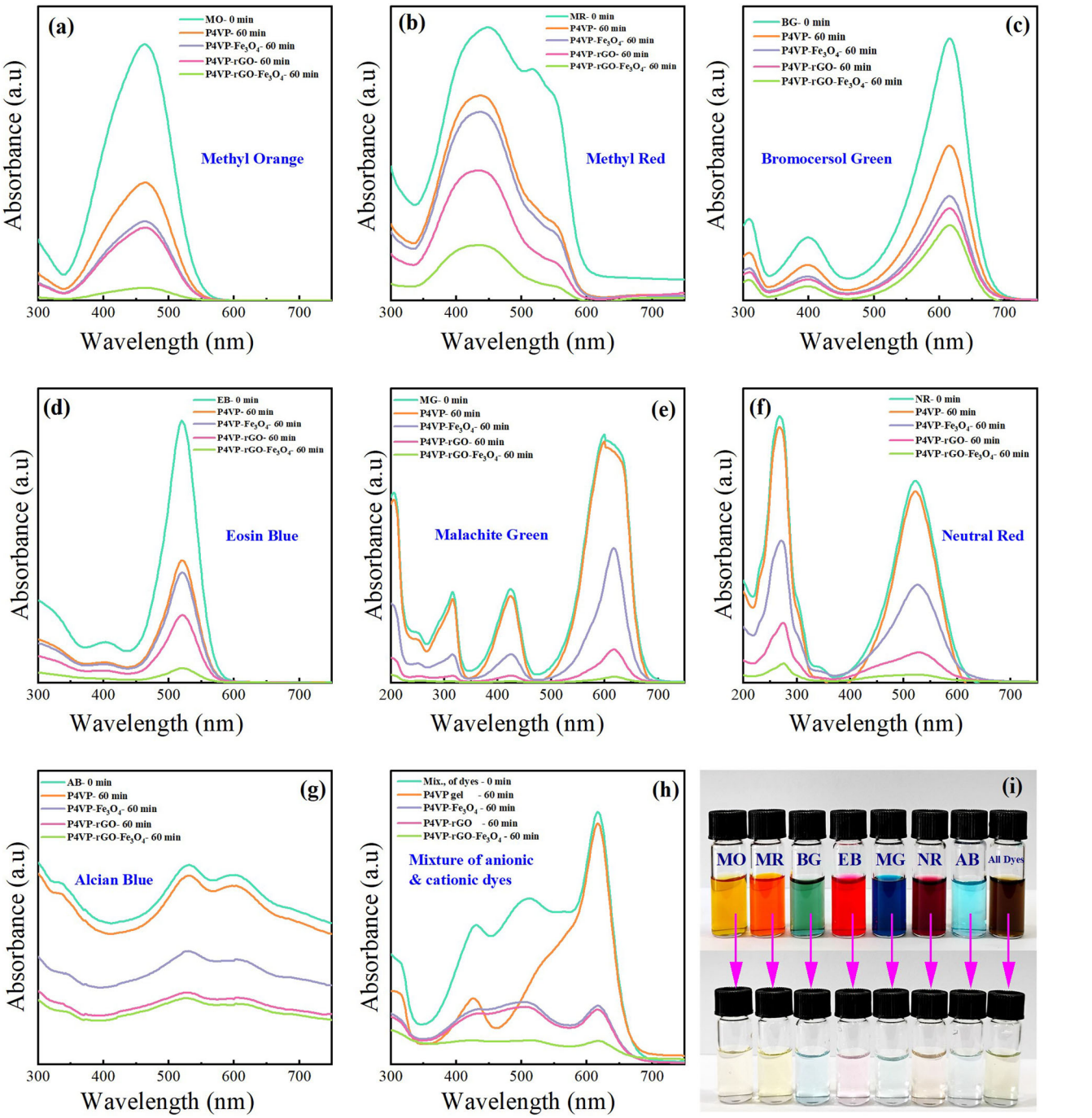

Fig. 4 | Time-evolution of the UV-vis spectra of the different dyes and the photograph of the dye solutions. UV-vis spectra of the dyes adsorbed by the four types of gels for a contact time of 60 min (**a**–**h**) and (**i**) photograph of the dye solution before and after adsorption by the P4VP-rGO-Fe_3O_4 OMG.

Adsorption kinetics and adsorption isotherms

Next, we determined the dye adsorption kinetics of all the gels. The relationship between adsorption capacity and time describes the rate at which dyes are adsorbed into an adsorbent. We applied three classical models: the Lagergren pseudo-first-order, Ho and McKay pseudo-second-order, and Weber-Morris intra-particle diffusion models to determine the adsorption kinetics. The selection of the kinetic model for the dye adsorption by the P4VP-rGO-Fe_3O_4 OMG was determined based on the R-squared (R^2) values, which indicate the goodness of fit for each model. Table. S2 presents the R^2 values obtained for the pseudo-first-order, pseudo-second-order, and Weber-Morris intra-particle diffusion models. Among these models, the pseudo-first-order kinetic model fits the data well, exhibits the highest R^2 value, and best describes the adsorption behavior of the P4VP-rGO-Fe_3O_4 OMG. Thus, the adsorption process is primarily governed by physisorption, characterized by weak van der Waals forces and rapid and reversible adsorption dynamics. The poor fit of the pseudo-second-order model suggests the limited role of chemisorption for all the dyes. Similarly, the Weber-Morris intra-particle diffusion model does not fit the data well. The kinetic study thus confirms that the P4VP-rGO-Fe_3O_4 OMG can rapidly adsorb, and the process is reversible, implying the possibility of faster adsorption and ease of regeneration of the adsorbent.

Information on the adsorption mechanisms and surface properties of adsorbents can be obtained from the adsorption isotherms. We utilized three commonly applied models, the Langmuir and Freundlich and the Sips

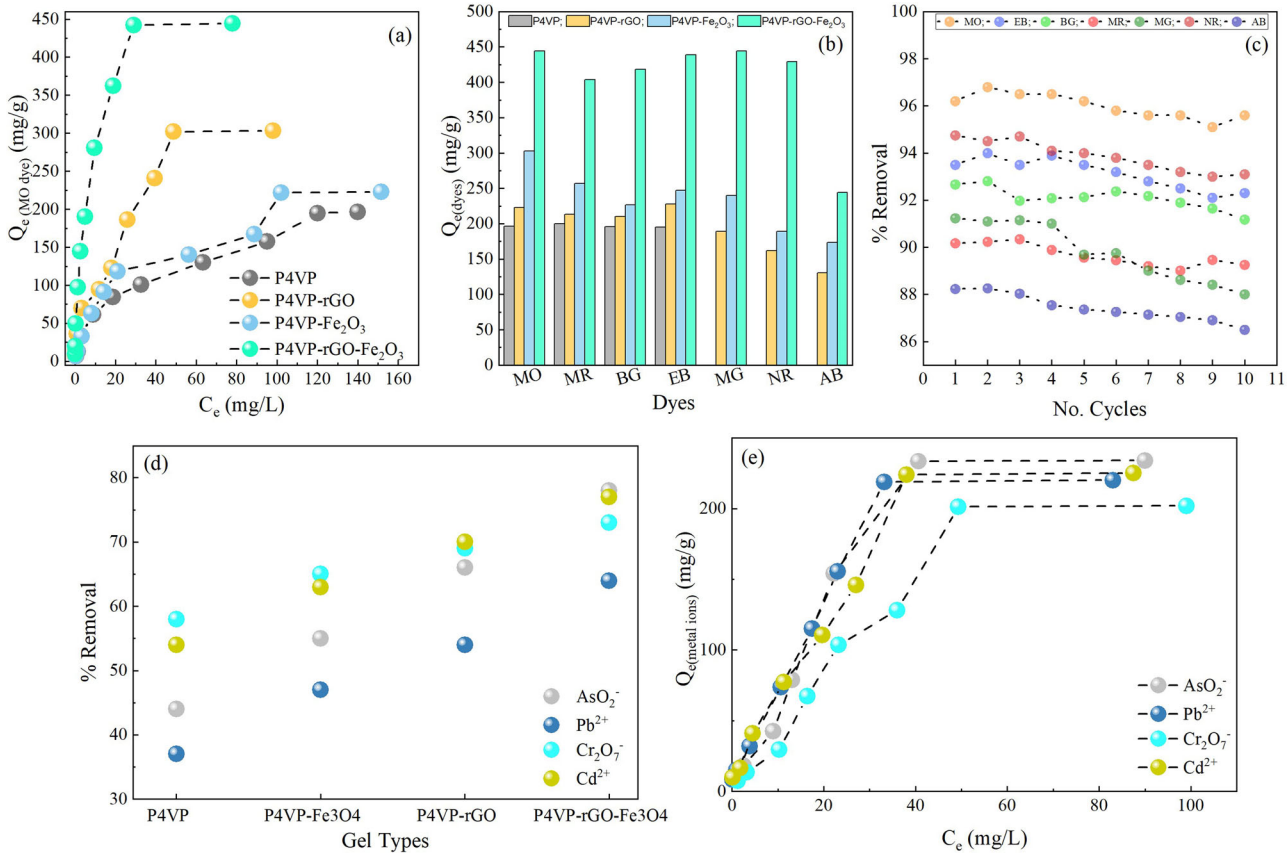

Fig. 5 | Adsorption capacity, removal efficiency for the dyes and heavy metals. $Q_{e(dyes)}$ (**a**) for various gels towards MO dye, **b** all gels towards different anionic and cationic dyes (**c**) removal efficiency of the P4VP-rGO-Fe_3O_4 organogel for the dyes as a function of the number of recycle times, **d** removal of heavy metal ions by the P4VP-rGO-Fe_3O_4 OMG and **e** $Q_{e(metal\ ions)}$ of the P4VP-rGO-Fe_3O_4 OMG towards different metal ions.

isotherms, to assess the adsorption behavior. The Langmuir model, described mathematically by Eq. 8, assumes monolayer adsorption on a homogeneous surface with a finite number of identical binding sites having equal energy and enthalpy. In contrast, the Freundlich model described by Eq. 9, accounts for adsorption on a heterogeneous surface, with binding sites exhibiting varying affinities and energies. The Sips model described by Eq. 10 combines the Langmuir and Freundlich isotherms, capturing both monolayer adsorption behavior and surface heterogeneity. In our study, the adsorption isotherms were generated by analyzing the equilibrium relationship between the equilibrium concentration (C_e), and the equilibrium adsorption capacity (Q_e) of the gels. The experimental data were plotted against all three models and fitted with the respective isotherms. The Sips model provided a better fit for the dye adsorption data for all the dyes, indicating that the adsorption process primarily occurs via monolayer adsorption on a heterogeneous surface. If $n = 1$, the adsorption is linear with a homogeneous surface (reduces to the Langmuir model); if $n < 1$, then the adsorption is favorable, and the surface heterogeneity increases. We obtained $n < 1$ in our fits, indicating the adsorption on a heterogeneous surface. The fitted values obtained for the Langmuir, Freundlich, and Sips adsorption isotherms are provided in Table. S3.

Understanding the thermodynamics of the adsorption process provides information on the affinity of the adsorbent for the adsorbate and the feasibility of an adsorption process. Here, we calculated the thermodynamic parameters (Eqs. 11 and 12) for dye adsorption for two cationic and two anionic dyes by the P4VP-rGO-Fe_3O_4 OMG. ΔH and ΔS were obtained from the slope and the intercept of the fits to the Van't Hoff equation (Eq. 13). The thermodynamic parameters calculated for all the dyes are tabulated in Table S4. The ΔG values are negative for all the dyes at all temperatures, reflecting a spontaneous adsorption process, and the adsorption is thermodynamically favorable. Moreover, as the temperature is raised from 30 to 60 °C, ΔG values were found to be increasingly negative for all the dyes, implying spontaneous adsorption at higher temperatures. The ΔH and ΔS values were positive at all temperatures for all the dyes. Positive values of ΔH imply that the adsorption process is endothermic. Positive values of ΔS imply that the degree of disorder during the adsorption at the solid-liquid (gel-dye solution) interface process is increasing. Among the four dyes chosen for the thermodynamic studies, MO shows the most negative ΔG value, implying it has the highest spontaneity of adsorption.

Regeneration, recycling and gel stability studies

The regeneration and reuse of adsorbents are crucial conditions for sustainable industrial scaling and reduction in secondary contamination. The P4VP-rGO-Fe_3O_4 OMG was specifically evaluated for its regeneration capability. After adsorbing the dyes, the gel was immersed in 5 mL of ethanol solution for 15 min and repeated until UV–vis spectroscopy confirmed that all detectable dye was effectively desorbed. The gel was then subjected to repeated adsorption experiments to assess its reusability. Regeneration and reuse tests were conducted over 10 cycles using both anionic and cationic dyes to validate the performance of the P4VP-rGO-Fe_3O_4 OMG. Remarkably, the P4VP-rGO-Fe_3O_4 OMG retained nearly 85% of its original dye removal efficiency even after multiple cycles, as illustrated in (Fig. 5c).

To assess the structural integrity of the OMG following 10 adsorption-desorption cycles, FTIR analysis was conducted after several washes post-adsorption (Fig. S5). The spectral features of OMG before and after reuse reveal that the OMG maintains its chemical structure with minimal degradation. The characteristic absorption bands attributed to C-N stretching (~1100 cm^{-1}) and C = N stretching (~1650 cm^{-1}) remain in the OMG even after adsorption, indicating the retention of these functional

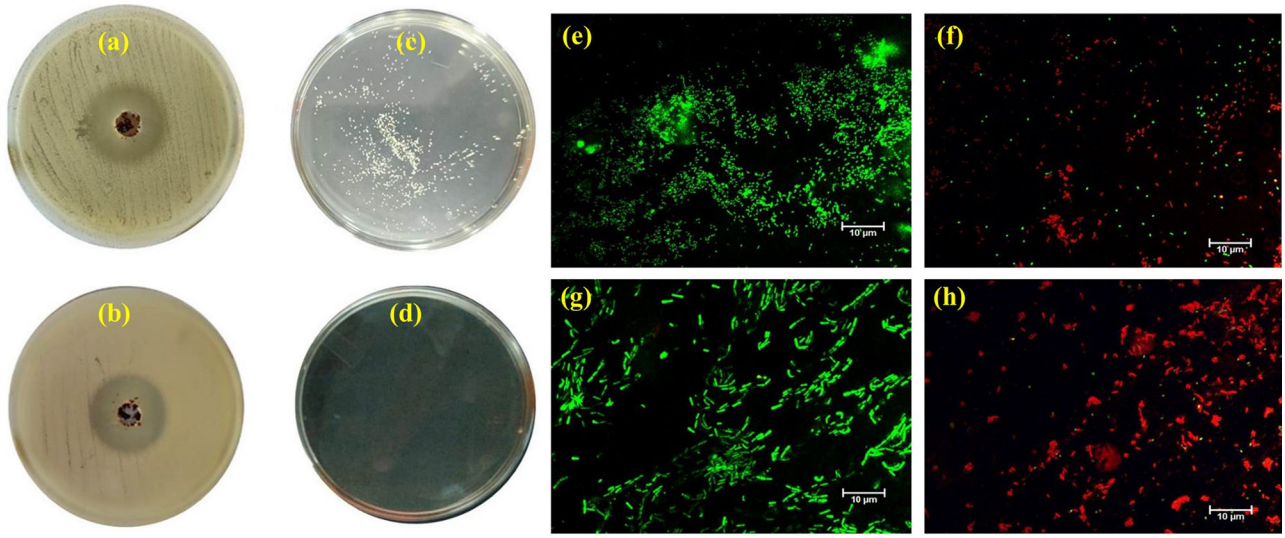

Fig. 6 | Well diffusion assay and total viability count. Well diffusion assay (**a**, **b**) and the total viability count (**c**, **d**) for *E. coli and S. Typhi*. Fluorescence microscopy of *E. coli* (**e**, **f**) and *S. Typhi* (**g**, **h**) stained with fluorescent cell viability marker (live/dead assay; acridine orange (AO) and propidium iodide (PI) staining). Green fluorescence (AO) represents live cells, while red fluorescence (PI) represents dead cells.

groups, which are very crucial for adsorption. Additionally, the aromatic C-H stretching band (~3450 cm^{-1}) persists with only a slight peak shift, suggesting the structural framework of the gel remains largely intact. The absence of significant shifts, peak broadening, or the emergence of new peaks further confirms the chemical stability of the OMG after repeated use.

The pH dependence of the adsorption process was evaluated using one anionic dye, MO, and one cationic dye, MG. The adsorption experiments were conducted at varying pH values after 60 min of contact time with the OMG, and the resulting UV-vis absorption spectra are shown in Fig. S6 (panel a for MO and panel b for MG). In the OMG, the bridging between pyridine and DBD forms a supramolecular network structure stabilized by electrostatic interactions. The pH-dependent adsorption behavior of MO and MG by the OMG is significantly influenced by the composite nature of OMG, which contains pyridinium groups, rGO, and Fe_3O_4. MO is an anionic azo dye, and MG is a cationic triphenylmethane dye. Both dyes display maximum adsorption at pH 3, with a gradual decline in removal efficiency as pH increases (Fig. S6). A similar trend, for MO and MG, indicates that the adsorption mechanism involves more than simple electrostatic interactions. Under acidic conditions, the OMG network becomes more protonated, enhancing hydrogen bonding potential and promoting a compact network structure. rGO imparts π-electron-rich domains that facilitate strong π–π stacking interactions with the aromatic rings of both MO and MG. Additionally, functional groups such as –OH and –COOH on rGO and surface hydroxyl groups on Fe_3O_4 can form hydrogen bonds and participate in polar interactions with the dye molecules. The positively charged pyridinium groups further contribute to π–π interactions rather than repulsion in the case of MG. At higher pH, partial deprotonation of these functional groups reduces the overall affinity of the OMG for both dyes. Collectively, the enhanced adsorption at low pH is driven by a combination of π–π stacking, hydrogen bonding, and OMG network-dye compatibility effects, rather than pure electrostatics.

Heavy metal removal studies

We also determined the adsorption efficiency of the gels towards heavy metal ions, such as arsenic (AsO_2^-), lead (Pb^{2+}), chromium ($Cr_2O_7^{2-}$), and cadmium (Cd^{2+}). The removal efficiencies exceeded 60% for the P4VP-rGO-Fe_3O_4 OMG (Fig. 5d). The $C_5H_5NH^+$ cations in P4VP facilitate strong electrostatic interactions with heavy metal ions such as AsO_2^- and $Cr_2O_7^{2-}$, and the divalent cations such as Pb^{2+} and Cd^{2+} can co-ordinate with the nitrogen in the pyridyl groups of P4VP forming a metal-ion complex. rGO and Fe_3O_4 contribute to a high surface area and abundant oxygenous groups[72], enhancing metal ion binding, and iron-based adsorbents are known to remove heavy metals[73]. The removal efficiency for the AsO_2^- ion was 44% with the P4VP organogel and 78% with P4VP-rGO-Fe_3O_4 OMG, while for lead (Pb^{2+}), it increased from 37 to 64%. Chromium ($Cr_2O_7^{2-}$) adsorption follows a similar trend, rising from 58% with P4VP to 73% with P4VP-rGO-Fe_3O_4 OMG, and cadmium (Cd^{2+}) with 54% to 77%. Among these materials, P4VP-rGO-Fe_3O_4 exhibits the highest overall adsorption performance. We also calculated the equilibrium adsorption capacity of the OMG for the heavy metal ions ($Q_{e(metal\ ions)}$) (Fig. 5e). The $Q_{e(metal\ ions)}$ was found to be 234, 220, 202, and 225 mg/g for the AsO^{2-}, Pb^{2+}, $Cr_2O_7^{2-}$, and Cd^{2+} ions, respectively. To further assess the practical applicability of the OMG, adsorption studies were performed using a mixed solution containing As, Pb, Cd, and Cr ions, for a total concentration of 100 ppm. After treatment with OMG, the final concentration of heavy metals was reduced to ~32 ppm, corresponding to an overall adsorption efficiency of ~68%. These results demonstrate the capability of OMG to effectively remove multiple heavy metal ions simultaneously from aqueous systems.

To evaluate the textural properties of the OMG, we performed nitrogen adsorption-desorption measurements, and the corresponding isotherm data are shown in Figure S7. The BET surface area was calculated to be 189.561 m^2/g, with a pore volume of 0.984 cm^3/g, a pore radius of 2.49 nm and an average pore width of 4.90 nm. These values indicate a mesoporous structure in the OMG that facilitates not only surface adsorption but also the entrapment, efficient diffusion and access of the pollutants into the interior of the OMG matrix.

Antibacterial activity studies

The zone of inhibition and the total viable count as a function of the P4VP-rGO-Fe_3O_4 OMG concentration for *E. coli* and *S. Typhi*, are shown in Fig. S8 and S9, respectively. In both bacterial species, 200 mg of gel pellets exhibited the most potent antibacterial effect, significantly inhibiting bacterial growth compared to all other concentrations. 200 mg of OMG is chosen for further antibacterial studies. Figure 6a, b shows the zone of inhibition on standard plate count agar and the total viable count colonies on Fig. 6c, d for *E. coli and S. Typhi*, respectively. A maximum zone inhibition of 28 ± 2 mm is measured for both *E. coli* and *S. Typhi*. Here, we used ampicillin, an antibiotic, as a control, and the corresponding zone of inhibition was measured to be about 15 ± 1 mm. A distinct difference in

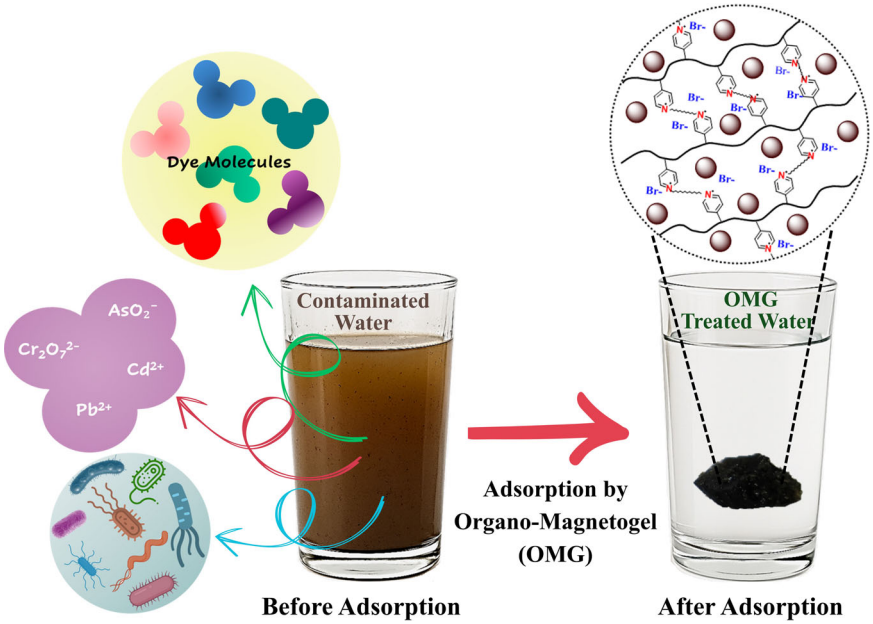

Fig. 7 | Action of the OMG towards pollutants. Illustration of the adsorption of various pollutants by the OMG.

susceptibility for the two bacterium was observed, while *E. coli* plates still exhibited colony formation, no colonies were detected on the *S. Typhi* plates. This indicates that *S. Typhi* is more susceptible to the OMG than *E. coli*. The enhanced inhibition could be attributed to differences in the bacterial cell wall structure and permeability or to the nature of interaction with the rGO-Fe_3O_4 composites in the gel.

To further assess the antimicrobial activity of the P4VP-rGO-Fe_3O_4 gel, a live/dead assay using acridine orange (AO) and propidium iodide (PI) staining was performed. AO stains live cells green, while PI stains dead cells red by entering cells with damaged membranes. The gel was removed after bacterial exposure, and the suspension was centrifuged at 3000 rpm for 10 min. The supernatant was discarded, and the pellet was washed with sterile phosphate-buffered saline (PBS). The pellet was resuspended in 1 mL of PBS, and AO and PI were added at final concentrations of 10 μg/mL and 5 μg/mL, respectively. The mixture was incubated at room temperature in the dark for 15 min to ensure dye penetration. A 10 μL sample of the stained suspension was placed on a glass slide, covered with a coverslip, and analyzed under a fluorescence microscope. Green fluorescence indicated live cells, while red fluorescence signified dead cells. A minimum of 200 cells per sample was counted to calculate the live-to-dead cell ratio. The live/dead images of *E. coli* and *S. Typhi* exposed to P4VP-rGO-Fe_3O_4 OMG are shown in Fig. 6e, f and Fig. 6g, h, respectively. Both the bacterial samples show negligible green fluorescence, indicating the non-survival of the bacteria.

E. coli and *S. Typhi* are prominent water-borne bacteria associated with water contamination. The effectiveness of the P4VP-rGO-Fe_3O_4 OMG in killing *E. coli* and *S. Typhi* can be attributed to its components. The pyridinium groups in P4VP possess inherent antibacterial properties, primarily by disrupting bacterial cell membranes through ionic interactions. The electrostatic attraction between the positively charged quaternary pyridinium ions and the negatively charged bacterial phospholipid layer, combined with the penetration of the hydrophobic vinyl chains into the bacterial membrane, destabilizes the membrane structure, resulting in bacterial death[74–76]. Fe_3O_4 particles enhance the antibacterial activity by generating reactive oxygen species (ROS), and the extent of ROS production increases proportionally to the Fe_3O_4 content[77]. ROS produced by graphene is also harmful to lipids and proteins in bacteria[78]. In the presence of ROS, the bacteria can no longer proliferate as the lipids and proteins are deactivated[78]. Molecular dynamics simulations[79] have shown that graphene can penetrate bacterial cell membranes by physically cutting through and inserting itself into the lipid bilayer. This results in the extraction of the phospholipid molecules from the bacterial cell membrane, resulting in loss of bacterial viability due to the strong interaction between membrane lipids and graphene. However, in our case, the antibacterial activity contribution from graphene arises solely from ROS, as the graphene sheets are not freely suspended but are instead encapsulated within the polymer network. The encapsulation of rGO and Fe_3O_4 within the P4VP gel creates a potent antibacterial material to effectively target and kill *E. coli* and *S. Typhi*.

In P4VP-rGO-Fe_3O_4 OMG, ~2 wt% of the total formulation corresponds to the rGO-Fe_3O_4 composite. Based on this, 200 mg of the OMG contains ~4 mg of the rGO-Fe_3O_4 composite. Given that the composite was prepared using a 3:1 weight ratio of reduced rGO to Fe_3O_4, the actual Fe_3O_4 content within the 200 mg of OMG will be 1 mg. Furthermore, the OMG immobilizes the rGO-Fe_3O_4 composite, potentially reducing nanoparticle leaching and environmental exposure risks compared to freely dispersed nanoparticles. Nevertheless, comprehensive ecotoxicological assessments, including toxicity tests on representative aquatic species, systematic toxicity evaluations in line with international frameworks such as OECD guidelines for testing chemicals and emerging nanomaterial risk assessments, are essential for future work to fully validate the environmental safety of the P4VP-rGO-Fe_3O_4 OMG for real-world water treatment applications.

The P4VP-rGO-Fe_3O_4 organo-magnetogel demonstrates exceptional potential as a multifunctional material for environmental remediation, addressing pollutant-contaminated water treatment. An illustration of the adsorption of the various pollutants by the OMG is provided in Fig. 7. In contrast to powder-based adsorbents that demand filtration for adsorbent recovery, the magnetic property of the OMG enables simple one-step separation after use. Additionally, unlike many framework materials that rely on complex synthesis protocols or expensive precursors, the OMG can be prepared under ambient conditions using a scalable and cost-effective process. With model dye pollutant adsorption capacities reaching as high as 444 mg/g, the P4VP-rGO-Fe_3O_4 OMG stands out as a top contender in handling pollutants. The gel effectively removes at least 60% of the toxic heavy metal ions, such as lead, arsenic, chromium, and cadmium. The antibacterial activity of the P4VP-rGO-Fe_3O_4 OMG is remarkable, exhibiting nearly complete eradication of *S. Typhi* bacteria. The combined attributes in OMG, broad-spectrum adsorption, magnetic recoverability, chemical stability, ease of regeneration, and scalable production, make the P4VP-

rGO-Fe_3O_4 OMG a promising next-generation material for a sustainable and efficient water treatment strategy.

Methods

General information

4-Vinylpyridine (98%, Sigma-Aldrich) was purified by passing it through an alumina column to remove the inhibitor. The initiator, 2,2′-azobis(2-methylpropionitrile) (AIBN, 98%, Sigma-Aldrich), was recrystallized from methanol before use. DBD (98%, Sigma-Aldrich) was used as the cross-linker. Graphite powder, sulfuric acid (H_2SO_4), potassium permanganate ($KMnO_4$), sodium nitrate ($NaNO_3$), hydrogen peroxide (H_2O_2), DMF, ferric chloride ($FeCl_3$), ferrous sulfate ($FeSO_4$), and ammonia solution 25% (NH_4OH) were sourced from Merck. Sodium arsenite ($NaAsO_2$), potassium dichromate ($K_2Cr_2O_7$), lead(II) nitrate ($Pb(NO_3)_2$) and cadmium chloride hemi-pentahydrate ($CdCl_2$ $2.5H_2O$) were used for heavy metal removal studies. The structure of the dyes used for the dye adsorption studies is provided in Fig. S4. All solvents and dyes were used as received.

Synthesis of reduced graphene oxide (rGO)

GO was prepared by exfoliating graphite flakes using a modified Hummers method[80,81]. Typically, 5 g of graphite flakes and 2 g of $NaNO_3$ were added to 20 mL of concentrated H_2SO_4 in a round-bottom flask. The reaction flask was maintained in ice-cold conditions. 3 g of $KMnO_4$ was slowly added into the reaction flask, taking precautions to keep the flask below 20 °C. The reactants were continuously stirred, and a purple-green mixture was obtained. The flask was then maintained at 35 °C and was continuously stirred for 12 h, yielding a dark brown paste. 50 mL of water was added to this paste and oxidized for another 96 h. The reaction was terminated by adding 50 mL of water and 5 mL of H_2O_2 (30%) solution. The resulting graphite oxide was dispersed in DI water and exfoliated using a probe sonicator to prepare the rGO dispersion[82].

Synthesis of magnetite (Fe_3O_4)

Fe_3O_4 particles were synthesized by aging a stoichiometric mixture of ferric chloride hexahydrate ($FeCl_3{\cdot}6H_2O$) (5.406 g) and ferrous sulfate ($FeSO_4$) (2.702 g) dissolved in 200 mL distilled water in a beaker. The mixture was heated to 60 °C and stirred continuously under a nitrogen atmosphere. After 1 h, 12 mL of ammonia (30%) solution was added. The solution colour changed from brown to black. The black precipitate was washed repeatedly with water and dried for 24 h.

Synthesis of poly(4-vinylpyridine) (P4VP) homopolymer

P4VP was synthesized via solution-free radical polymerization by dissolving 4-vinylpyridine and AIBN in DMF in a round-bottom flask; schematic of the synthesis is given in Fig. 1. The reaction was carried out at 70 °C for 24 h under an inert atmosphere. The P4VP polymer was precipitated from cold diethyl ether and repeatedly washed using a cold water/hexane mixture to remove the unreacted monomers. The resultant polymer was stored under a vacuum.

Dye adsorption experiments and reusability of organogels

Dye adsorption studies were conducted using OMG pellets in solutions containing anionic, cationic, and mixed anionic-cationic dyes. The gel pellets, each weighing 20 mg, were prepared by cutting sections from the bulk organogel. The anionic dyes used in this study were MO, MR, EB, and BG. The cationic dyes were NR, AB, and MG. All dye solutions were prepared at a concentration of 0.1 g/L. The adsorption process was monitored by measuring the UV–Vis absorption spectra at 15-min intervals after introducing the organogel into the dye solution. The remaining dye concentration in the solution was quantified based on the UV–vis data. To evaluate regeneration, the dye-loaded organogel was soaked in 5 mL of ethanol for 10 min to remove the dye. The organogel was then dried and reused for multiple dye adsorption and removal cycles to validate its reusability. Equilibrium adsorption experiments were carried out to ensure adsorption equilibrium. The equilibrium adsorption capacity ($Q_{e\ dyes}$, mg/g) was determined using the relation[21,83,84],

$$Q_{e\,dyes} = \frac{(C_{o-}C_e)}{m} \times V \tag{1}$$

where C_o and C_e are the initial and equilibrium dye concentration, respectively, V is the volume of the dye solution, and m is the weight of the adsorbent.

The dye removal efficiency (R, %) was calculated using Eq. 2. After removing the P4VP-rGO-Fe_3O_4 organogel from the dye solution, it was soaked in a mixture of ethanol for 15 min to desorb the dye and washed with water and followed by dye adsorption. This adsorption-desorption procedure was repeated 10 times to evaluate the reusability of the organogel.

The dye removal efficiency (R, %) of the organogel was calculated using the following equation[21],

$$R\% = 100 \times \frac{C_i - C_f}{C_i} \tag{2}$$

where C_i and C_f are the initial and final concentrations (mg/L) of the dye in the solution before and after adsorption.

The Lagergren pseudo-first-order kinetics is given by,

$$\frac{dQ_t}{dt} = k_1(Q_e - Q_t) \tag{3}$$

Here, Q_t is the amount of adsorbate adsorbed at time t (mg/g), Q_e is the amount of adsorbate adsorbed at equilibrium (mg/g), k_1 is the pseudo-first-order rate constant (min^{-1}) and t is the time (min). The integral form of Eq. 3, can be expressed as,

$$ln(Q_e - Q_t) = lnQ_e - k_1 t \tag{4}$$

The Ho and McKay pseudo-second-order kinetics follows,

$$\frac{dQ_t}{dt} = k_2(Q_e - Q_t)^2 \tag{5}$$

Here k_2 is the pseudo-second-order rate constant (g mg^{-1} min^{-1}), and the linear form of Eq. 5, can be written as,

$$\frac{t}{Q_t} = \left(\frac{1}{k_2 Q_e^2}\right) + \frac{t}{Q_e} \tag{6}$$

The Weber-Morris model is given by,

$$Q_t = k_i t^{0.5} + B \tag{7}$$

Here, k_i is the intra-particle diffusion rate constant (mg/g.$min^{0.5}$) and B (mg/g) is the intercept.

The expression for the Langmuir, Freundlich and Sips isotherms are given in Eq. 8, Eq. 9 and Eq. 10.

$$\frac{C_e}{Q_e} = \frac{1}{Q_m} \times C_e + \frac{1}{K_L Q_m} \tag{8}$$

$$lnQ_e = \frac{1}{n} \times lnC_e + lnK_F \tag{9}$$

$$Q_e = \frac{Q_m (K_S C_e)^{\frac{1}{n}}}{1 + (K_S C_e)^{\frac{1}{n}}} \tag{10}$$

where C_e is the equilibrium dye concentration, Q_e is the equilibrium adsorption capacity, Q_m is the maximum adsorption capacity, K_L, K_F and K_S are the Langmuir, Freundlich and Sips adsorption constants, and $1/n$ infers how favourable the adsorption process is.

The Gibbs free energy ΔG (kJ/mol), enthalpy (ΔH) (kJ/mol), and entropy (ΔS) (J/K.mol) are related by,

$$\Delta G = \Delta H - T\Delta S \tag{11}$$

$$\Delta G = -RT\ lnk_e \tag{12}$$

By combining Eq. 11, and Eq.12, we get the linear form of the Van't Hoff equation

$$lnk_e = -\frac{\Delta H}{RT} + \frac{\Delta S}{RT} \tag{13}$$

Here, R is the ideal gas constant (8.314 J/K·mol), T is the temperature, K_e is the equilibrium constant.

Zone of inhibition (ZOI) assay and total viable count

The antimicrobial activity of P4VP-rGO-Fe_3O_4 gel was evaluated using the zone of inhibition (ZOI) assay at different concentrations (50, 100, 150, and 200 mg) against *E. coli* and *S. Typhi*. A bacterial suspension standardized to 10^6–10^8 CFU/mL was uniformly spread on nutrient agar plates using sterile cotton swabs. Wells ~6 mm in diameter were created on the agar, and each was loaded with the gel at the specified concentrations. The plates were incubated at 37 °C for 24 h to promote bacterial growth and allow for assessment of the antimicrobial effects. After incubation, the clear zones around the wells were measured in millimeters to determine the extent of bacterial growth inhibition. The antimicrobial effectiveness of the P4VP-rGO-Fe_3O_4 composite was tested against *E. coli* and *S. Typhi*, both sourced from a microbiological repository. Bacteria were cultured in Luria Bertani Broth (LB) at 37 °C for 18–24 h. The cultures were adjusted to a concentration of 10^6–10^8 CFU/mL by measuring the optical density at 600 nm (OD_{600}) and confirming via serial dilution and agar plating.

Techniques

The molecular weight (61 KDa) and polydispersity (1.32) of the poly(4-vinylpyridine) (P4VP) were determined using a Waters Acquity Advanced Polymer Chromatography (APC) system, here DMF was used as the eluent at a flow rate of 0.5 mL/min. Proton nuclear magnetic resonance (^{1}H NMR) analysis was performed on a JEOL 400 MHz spectrometer, using $CDCl_3$ as the solvent. The morphology and elemental composition of the organogel and powder samples were analyzed using a ThermoFisher Scientific Quattro S field emission environmental scanning electron microscope (ESEM), which is operated jointly by the Helmholtz-Zentrum Hereon and the Jülich Center for Neutron Science (JCNS) at Heinz Maier-Leibnitz Zentrum (MLZ). In ESEM mode, the water-vapor partial pressure in the chamber was set to 100 Pa to avoid charging. A circular backscattered detector (CBS) was used, and the images were taken at an acceleration voltage of 12 kV and a probe current of 1.2 nA. In high vacuum mode, the samples were previously sputter coated with 5 nm Pt/Pd 80/20. Here, the images were taken at 22 kV and 35 pA with an Evenhart-Thornley secondary electron detector (ETD). In addition, energy-dispersive X-ray spectroscopy was carried out for mapping elemental composition with a ThermoFisher EDS UltraDry-Si-drift detector (60 mm²) at a take-off angle of 40° with an energy resolution of 127 eV Mn Kα at an e-beam emission current of 500 pA. An acceleration voltage of 12 kV and a probe current of 1.1 nA was used, resulting in a count rate of 15 kcps and a dead time of 5% during 15 min of integration. SAXS measurements were carried out using the laboratory-based SAXS beamline KWS-X (XENOCS XUESS 3.0 XL) at JCNS MLZ. The experiments utilized Excillum MetalJet D2+ MetalJet X-ray source with a liquid metal anode, operating at 70 kV and 3.57 mA, emitting Ga-Kα radiation with a wavelength of 1.314 Å. The gel samples were placed in glass capillaries with a 2 mm inner diameter at room temperature (~25 °C). The sample-to-detector distances varied from 0.5 m to 1.70 m, corresponding to a scattering vector q range of 0.003 to 1 Å^{-1}. The collected SAXS patterns were normalized on an absolute scale, azimuthally averaged to derive intensity profiles, and corrected by subtracting the background. Dye adsorption, gel stability studies and heavy metal removal studies were carried out using a UV-vis-NIR spectrophotometer (JASCO V-670, Japan) and an atomic absorption spectrometer (iCE-FIOS, Thermo Scientific), respectively. The room temperature magnetic properties of Fe_3O_4 and the P4VP-rGO-Fe_3O_4 OMG were measured with a Lakeshore 7410S vibrating sample magnetometer (VSM). The Brunauer-Emmett-Teller (BET) surface area, pore volume, and pore size distribution were measured using a Quantachrome Instruments gas sorption analyzer (version 5.23) equipped for automated surface area and pore structure analysis.

Data availability

Data is provided within the manuscript or supplementary information files.

Received: 26 April 2025; Accepted: 28 June 2025;
Published online: 25 July 2025

References

1. Bayramoglu, G., Kunduzcu, G. & Arica, M. Y. Preparation and characterization of strong cation exchange terpolymer resin as effective adsorbent for removal of disperse dyes. *Polym. Eng. Sci.* **60**, 192–201 (2020).
2. Pereira, I. C. et al. Thermal and thermal-acid treated sewage sludge for the removal of dye reactive Red 120: characteristics, kinetics, isotherms, thermodynamics and response surface methodology design. *J. Environ. Chem. Eng.* **6**, 7233–7246 (2018).
3. Silva, T. L. et al. Mesoporous activated carbon from industrial laundry sewage sludge: adsorption studies of reactive dye Remazol Brilliant Blue R. *Chem. Eng. J.* **303**, 467–476 (2016).
4. Sonai, G. G., de Souza, S. M. A. G. U., de Oliveira, D. & de Souza, A. A. U. The application of textile sludge adsorbents for the removal of Reactive Red 2 dye. *J. Environ. Manag.* **168**, 149–156 (2016).
5. Jung, K. W., Lee, S. Y. & Lee, Y. J. Optimized preparation of activated carbon from municipal sewage sludge and application to the adsorption of azo dye from aqueous solutions. *Environ. Prog. Sustain. Energy* **38**, S267–S276 (2019).
6. Tang, J. et al. Heavy metal pollution level and potential ecological risk assessment of sludge landfill. *Environ. Prog. Sustain. Energy* **41**, e13795 (2022).
7. Juel, M. A. I., Noyon, M. A. R., Mizan, A., Hashem, M. A. & Azam, M. G. Phytoextraction of heavy metals from tannery sludge: a cleaner approach. *Environ. Prog. Sustain. Energy* **41**, e13928 (2022).
8. Li, M. et al. Kirkendall effect boosts phosphorylated nzvi for efficient heavy metal wastewater treatment. *Angew. Chem. Int. Ed.* **60**, 17115–17122 (2021).
9. Li, Z. et al. Triboelectrification-enabled self-powered detection and removal of heavy metal ions in wastewater. *Adv. Mater.* **28**, 2983–2991 (2016).
10. Thompson, R. C. et al. Twenty years of microplastic pollution research-what have we learned? *Science* **386**, eadl2746 (2024).
11. Das, T. K., Basak, S. & Ganguly, S. 2D nanomaterial for microplastic Removal: a critical review. *Chem. Eng. J.* **492**, 152451 (2024).
12. Fork, M. L., Fick, J. B., Reisinger, A. J. & Rosi, E. J. Dosing the coast: leaking sewage infrastructure delivers large annual doses and dynamic mixtures of pharmaceuticals to urban rivers. *Environ. Sci. Technol.* **55**, 11637–11645 (2021).
13. He, Y., Zhang, Y. & Ju, F. Metformin contamination in global waters: biotic and abiotic transformation, byproduct generation and toxicity, and evaluation as a pharmaceutical indicator. *Environ. Sci. Technol.* **56**, 13528–13545 (2022).

14. Mondol, M. M. H. & Jhung, S. H. Adsorptive removal of pesticides from water with metal–organic framework-based materials. *Chem. Eng. J.* **421**, 129688 (2021).
15. Ushavipinachandran, V. et al. Detoxification of endocrine disruptors in water using visible-light-active nanostructures: a review. *ACS Appl. Nano. Mater.* **3**, 11659–11687 (2020).
16. Laubscher, B. et al. Multiple neonicotinoids in children's cerebrospinal fluid, plasma, and urine. *Environ. Health* **21**, 10 (2022).
17. Yang, Y. et al. Detection of various microplastics in patients undergoing cardiac surgery. *Environ. Sci. Technol.* **57**, 10911–10918 (2023).
18. Chigwechokha, P. et al. *Vibrio cholerae* and *Salmonella Typhi* culture-based wastewater or non-sewered sanitation surveillance in a resource-limited region. *J. Expo. Sci. Environ. Epidemiol.* **34**, 432–439 (2024).
19. Nowicki, S., DeLaurent, Z. R., De Villiers, E. P., Githinji, G. & Charles, K. J. The utility of *Escherichia coli* as a contamination indicator for rural drinking water: evidence from whole genome sequencing. *PLoS ONE* **16**, e0245910 (2021).
20. Sridhar, S. P. et al. Chemically crosslinked poly(N-isopropylacrylamide-block-4-vinylpyridine) organogel with myriad applications. *Mater. Lett.* **272**, 127854 (2020).
21. Sridhar, S. P. et al. Adsorption of anionic dyes using a poly(styrene-block-4-vinylpyridine) block copolymer organogel. *Langmuir* **37**, 3996–4006 (2021).
22. Rizzo, C. et al. Self-sustaining supramolecular ionic liquid gels for dye adsorption. *ACS Sustain. Chem. Eng.* **6**, 12453–12462 (2018).
23. Wang, Z. et al. Bioinspired supramolecular slippery organogels for controlling pathogen spread by respiratory droplets. *Adv. Funct. Mater.* **31**, 2102888 (2021).
24. Cheng, N., Hu, Q., Guo, Y., Wang, Y. & Yu, L. Efficient and selective removal of dyes using imidazolium-based supramolecular gels. *ACS Appl. Mater. Interfaces* **7**, 10258–10265 (2015).
25. Ganiyu, S. O., Martínez-Huitle, C. A. & Oturan, M. A. Electrochemical advanced oxidation processes for wastewater treatment: advances in formation and detection of reactive species and mechanisms. *Curr. Opin. Electrochem.* **27**, 100678 (2021).
26. Chanikya, P., Nidheesh, P. V., Syam Babu, D., Gopinath, A. & Suresh Kumar, M. Treatment of dyeing wastewater by combined sulfate radical based electrochemical advanced oxidation and electrocoagulation processes. *Sep. Purif. Technol.* **254** (2021).
27. Luo, H., Zeng, Y., He, D. & Pan, X. Application of iron-based materials in heterogeneous advanced oxidation processes for wastewater treatment: a review. *Chem. Eng. J.* **407**, 127191 (2021).
28. Zheng, Y. et al. Positively charged thin-film composite hollow fiber nanofiltration membrane for the removal of cationic dyes through submerged filtration. *Desalination* **328**, 42–50 (2013).
29. Lončarević, D., Dostanić, J., Radonjić, V., Živković, L. & Jovanović, D. M. Simultaneous photodegradation of two textile dyes using TiO2 as a catalyst. *React. Kinet. Mech. Catal.* **118**, 153–164 (2016).
30. Lučić Škorić, M. et al. Chitosan-based microparticles for immobilization of TiO_2nanoparticles and their application for photodegradation of textile dyes. *Eur. Polym. J.* **82**, 57–70 (2016).
31. Wang, F. et al. Facile synthesis of a Ag(i)-doped coordination polymer with enhanced catalytic performance in the photodegradation of azo dyes in water. *J. Mater. Chem. A Mater.* **3**, 5908–5916 (2015).
32. Sreedhar, M., Neelakanta Reddy, I., Reddy, C. V., Shim, J. & Brijitta, J. Highly photostable Zn-doped TiO2 thin film nanostructures for enhanced dye degradation deposited by sputtering method. *Mater. Sci. Semicond. Process* **85**, 113–121 (2018).
33. Li, Y., Lu, H., Wang, Y., Zhao, Y. & Li, X. Efficient removal of methyl blue from aqueous solution by using poly(4-vinylpyridine)–graphene oxide–Fe 3 O 4 magnetic nanocomposites. *J. Mater. Sci.* **54**, 7603–7616 (2019).
34. Das, T. K. & Poater, A. Review on the use of heavy metal deposits from water treatment waste towards catalytic chemical syntheses. *Int. J. Mol. Sci.* **22**, 13383 (2021).
35. Yang, W., Shirazian, S., Soltani, R. & Zare, M. H. Bio-originated mesosilicate SBA-15: synthesis, characterization, and application for heavy metal removal. *NPJ Clean Water* **7**, 49 (2024).
36. Kobylinska, N. G., Kessler, V. G., Seisenbaeva, G. A. & Dudarko, O. A. In situ functionalized mesoporous silicas for sustainable remediation strategies in removal of inorganic pollutants from contaminated environmental water. *ACS Omega* **7**, 23576–23590 (2022).
37. Kaur, H. et al. Metal-organic framework-based materials for wastewater treatment: superior adsorbent materials for the removal of hazardous pollutants. *ACS Omega* **8**, 9004–9030 (2023).
38. Song, Y., Phipps, J., Zhu, C. & Ma, S. Porous materials for water purification. *Angew. Chem. Int. Ed.* **62**, e202216724 (2023).
39. Engineering green MOF-based superhydrophobic sponge for efficiently synchronous removal of microplastics and pesticides from high-salinity water. **243**, 120314 (2023).
40. Zhao, R. et al. Constructing mesoporous adsorption channels and MOF-polymer interfaces in electrospun composite fibers for effective removal of emerging organic contaminants. *ACS Appl. Mater. Interfaces* **13**, 755–764 (2021).
41. Rojas, S. & Horcajada, P. Metal-organic frameworks for the removal of emerging organic contaminants in water. *Chem. Rev.* **120**, 8378–8415 (2020).
42. Jrad, A. et al. Cationic covalent organic framework for the fluorescent sensing and cooperative adsorption of perfluorooctanoic acid. *Nat. Commun.* **15**, 10490 (2024).
43. Ghahari, A., Farzad, F. & Azadnejad, R. The strategy of three-dimensional covalent organic frameworks to exclude dye contaminants in aqueous solutions. *NPJ Clean Water* **7**, 27 (2024).
44. Liu, X. et al. Orderly porous covalent organic frameworks-based materials: superior adsorbents for pollutants removal from aqueous solutions. *Innovation* **2**, 100076 (2021).
45. Akhzari, S., Raissi, H. & Ghahari, A. Architectural design of 2D covalent organic frameworks (COFs) for pharmaceutical pollutant removal. *NPJ Clean Water* **7**, 31 (2024).
46. Liu, T. et al. Covalent organic framework membrane for efficient removal of emerging trace organic contaminants from water. *Nat. Water* **1**, 1059–1067 (2023).
47. Alsawy, T., Rashad, E., El-Qelish, M. & Mohammed, R. H. A comprehensive review on the chemical regeneration of biochar adsorbent for sustainable wastewater treatment. *NPJ Clean Water* **5**, 29 (2022).
48. He, M. et al. Waste-derived biochar for water pollution control and sustainable development. *Nat. Rev. Earth Environ.* **3**, 444–460 (2022).
49. Karmakar, A. et al. Highly efficient adsorptive removal of organic dyes from aqueous solutions using polyaromatic group-containing Zn(II)-based coordination polymers. *Cryst. Growth Des.* **22**, 2248–2265 (2022).
50. Klemes, M. J. et al. Polymerized molecular receptors as adsorbents to remove micropollutants from water. *Acc. Chem. Res.* **53**, 2314–2324 (2020).
51. Liu, X. et al. Installation of synergistic binding sites onto porous organic polymers for efficient removal of perfluorooctanoic acid. *Nat. Commun.* **13**, 2132 (2022).
52. Wang, Z. Q., Wang, X. & Yang, Y. W. Pillararene-based supramolecular polymers for adsorption and separation. *Adv. Mater.* **36**, 2301721 (2024).
53. Li, M. et al. Self-assembling fluorescent hydrogel for highly efficient water purification and photothermal conversion. *Chem. Eng. J.* **431**, 134245 (2022).
54. Yang, Z. et al. Effective adsorption of arsenate, dyes and eugenol from aqueous solutions by cationic supramolecular gel materials. *Colloids Surf. A Physicochem. Eng. Asp.* **616**, 126238 (2021).

55. Takeshita, J. et al. Organic dye adsorption by amphiphilic tris-urea supramolecular hydrogel. *Chem. Asian J.* **12**, 2029–2032 (2017).
56. Guo, Z. et al. Giant microgels with CO2-induced on-off, selective, and recyclable adsorption for anionic dyes. *ACS Appl. Mater. Interfaces* **10**, 38073–38083 (2018).
57. Wei, R. et al. Bidirectionally pH-responsive zwitterionic polymer hydrogels with switchable selective adsorption capacities for anionic and cationic dyes. *Ind. Eng. Chem. Res.* **57**, 8209–8219 (2018).
58. Hu, M., Xie, N., Huang, Y. & Yu, Y. A super-efficient gel adsorbent with over 1000 times the adsorption capacity of activated carbon. *NPJ Clean Water* **7**, 50 (2024).
59. Hu, M., Xie, N., Gao, S., Huang, Y. & Yu, Y. A super-efficient polyquaternium gel that can remove over-10-times masses of lignins from wastewater for resourcefulness. *NPJ Clean Water* **6**, 2 (2023).
60. Morisada, S., Rin, T., Ogata, T., Kim, Y. H. & Nakano, Y. Adsorption removal of boron in aqueous solutions by amine-modified tannin gel. *Water Res.* **45**, 4028–4034 (2011).
61. Krishna Kumar, A. S. et al. Heavy metal and organic dye removal via a hybrid porous hexagonal boron nitride-based magnetic aerogel. *NPJ Clean Water* **5**, 24 (2022).
62. Jia, X., Peydayesh, M., Huang, Q. & Mezzenga, R. Amyloid fibril templated MOF aerogels for water purification. *Small* **18**, e2105502 (2022).
63. Li, Q. et al. Correlation between particle size/domain structure and magnetic properties of highly crystalline Fe_3O_4 nanoparticles. *Sci. Rep.* **7**, 9894 (2017).
64. Kemp, S. J., Ferguson, R. M., Khandhar, A. P. & Krishnan, K. M. Monodisperse magnetite nanoparticles with nearly ideal saturation magnetization. *RSC Adv.* **6**, 77452–77464 (2016).
65. Ding, W. et al. Ballistic cluster-cluster aggregation model optimization. *AIP Adv.* **13**, 035017 (2023).
66. Lazzari, S., Nicoud, L., Jaquet, B., Lattuada, M. & Morbidelli, M. Fractal-like structures in colloid science. *Adv. Colloid Interface Sci.* **235**, 1–13 (2016).
67. Shibayama, M. Structure-mechanical property relationship of tough hydrogels. *Soft Matter* **8**, 8030–8038 (2012).
68. McCoy, T. M. et al. Bulk properties of aqueous graphene oxide and reduced graphene oxide with surfactants and polymers: adsorption and stability. *Phys. Chem. Chem. Phys.* **20**, 16801–16816 (2018).
69. Liu, F., Chung, S., Oh, G. & Seo, T. S. Three-dimensional graphene oxide nanostructure for fast and efficient water-soluble dye removal. *ACS Appl. Mater. Interfaces* **4**, 922–927 (2012).
70. Xiao, J. et al. Environmentally friendly reduced graphene oxide as a broad-spectrum adsorbent for anionic and cationic dyes: via π-π Interactions. *J. Mater. Chem. A Mater.* **4**, 12126–12135 (2016).
71. Bradder, P., Ling, S. K., Wang, S. & Liu, S. Dye adsorption on layered graphite oxide. *J. Chem. Eng. Data* **56**, 138–141 (2011).
72. Guo, T. et al. Mechanism of Cd(II) and Cu(II) adsorption onto few-layered magnetic graphene oxide as an efficient adsorbent. *ACS Omega* **6**, 16535–16545 (2021).
73. Leitzke, T. J. et al. Water treatment method for removal of select heavy metals and nutrient ions through adsorption by magnetite. *ACS ES T Water* **2**, 1584–1592 (2022).
74. Ma, X. et al. Cationic 4-vinylpyridine copolymer nanospheres with dual active centers for antibacterial coatings. *ACS Appl. Nano. Mater.* **7**, 21083–21093 (2024).
75. Gokkaya Ozburun, D. et al. Quaternized poly(4-vinylpyridine-co-N-2-hydroxypropylmethacrylamide) and antibacterial peptide linear conjugates: synthesis, characterization, and bioactivity. *Eur. Polym. J.* **222** (2025).
76. Li, Q. et al. Fabrication of charge reversible graphene oxide-based nanocomposite with multiple antibacterial modes and magnetic recyclability. *J. Colloid Interface Sci.* **511**, 285–295 (2018).
77. Bajpai, I., Balani, K. & Basu, B. Synergistic effect of static magnetic field and HA-Fe3O 4 magnetic composites on viability of S. aureus and E. coli bacteria. *J. Biomed. Mater. Res. B Appl. Biomater.* **102**, 524–532 (2014).
78. Shi, L. et al. The antibacterial applications of graphene and its derivatives. *Small* **12**, 4165–4184, (2016).
79. Tu, Y. et al. Destructive extraction of phospholipids from Escherichia coli membranes by graphene nanosheets. *Nat. Nanotechnol.* **8**, 594–601 (2013).
80. Marcano, D. C. et al. Improved synthesis of graphene oxide. *ACS Nano* **4**, 4806–4814 (2010).
81. Bannov, A. G. et al. Synthesis and studies of properties of graphite oxide and thermally expanded graphite. *Prot. Met. Phys. Chem. Surf.* **50**, 183–190 (2014).
82. Dam, D. T., Wang, X. & Lee, J. M. Graphene/NiO nanowires: Controllable one-pot synthesis and enhanced pseudocapacitive behavior. *ACS Appl. Mater. Interfaces* **6**, 8246–8256 (2014).
83. Guo, Z. et al. Giant microgels with CO_2 -induced on-off, selective, and recyclable adsorption for anionic dyes. *ACS Appl. Mater. Interfaces* **10**, 38073–38083 (2018).
84. Qin, Y. et al. Ammonium-functionalized hollow polymer particles as a pH-responsive adsorbent for selective removal of acid dye. *ACS Appl. Mater. Interfaces* **8**, 16690–16698 (2016).

Acknowledgements

B.J. thanks the European Union's Horizon 2020 research and innovation program under the Marie Skłodowska-Curie grant agreement No 101034266.

Author contributions

S.P.S. synthesized the gels, conducted the dye and heavy metal adsorption studies, and performed data evaluation and literature analysis. S.U. and V.P. conducted antibacterial investigations. L.P. assisted with experimental work and data analysis. A.K. performed the SEM imaging, B.W. performed the SAXS measurements, and D.S. analyzed and fitted the SAXS data. J.V. and B.V. assisted in the dye adsorption experiments. A.R. and S.F. supported the analytical work through constructive discussions. B.J. contributed to the data interpretation and manuscript preparation. S.P.S. and B.J. co-wrote the manuscript with input from all co-authors.

Funding

Open Access funding enabled and organized by Projekt DEAL.

Competing interests

The authors declare no competing interests.

Additional information

Supplementary information The online version contains supplementary material available at https://doi.org/10.1038/s41545-025-00496-w.

Correspondence and requests for materials should be addressed to Brijitta Joseph.